Towards a Complete Numerical Description of Lubricant Film Dynamics in Ball Bearings

Stefan Knauf *   Stefan Frei[†]   Thomas Richter[†]   Rolf Rannacher[†]

Abstract

In this article, we propose a framework for a detailed finite element analysis of elastohydrodynamic lubrication in ball bearings. Our contribution to this field is twofold. First, we present a fully monolithic ALE method for the treatment of fluid-structure interaction. For the lubricant, we use the full Navier-Stokes equations in combination with a pressure-dependent viscosity law and include thermal effects. Second, we introduce a novel method for a fully implicit treatment of the evolution of the lubricants' free surface using Nitsches method. This allows for arbitrarily large time steps independent of the spatial discretization. Despite the variety of numerical challenges present in this application, such as anisotropy and extreme values of pressure, our approach for the first time shows robustness up to high rotational speeds as required in industrial applications. We describe the numerical ingredients we use in detail and present numerical results that validate our approaches and demonstrate its capabilities.

1 Introduction

In this article, we present numerical methods for the simulation of lubrication flow in bearings including fluid-structure interaction. In the literature this is referred to as "elastohydrodynamic lubrication" (EHL) and is considered as a particularly difficult topic embracing several disciplines (see, e.g., Gohar[17]). We are especially interested in the design of an efficient and robust numerical scheme for high rotational speeds, as occuring, e.g., in machines, turbines and space applications. In such high-speed applications, typically the high pressure leads to deformation of the surrounding structures. These deformations are relatively small compared to the size of a ball, but might reach the same order of magnitude as the lubrication film thickness itself. Hence, the domain occupied by the lubricant strongly depends on the deformation of ball and race. On the other hand, even small changes in the shape of the fluid domain lead to a large response in the pressure profile. Hence, including fluid-structure interactions plays an important role that should not be neglected in simulations. In order to treat this interaction implicitly, we propose a monolithic *Arbitrary Lagrangian Eulerian (ALE)* formulation (see, e.g., Hirt, Amsden & Cook[23], Belytschko[8], Hron & Turek[24], and Dunne et al.[14]).

For the lubricant, we consider a generalized Newtonian fluid modelled by the Navier-Stokes equations with pressure-dependent viscosity. Until recently, research in this field has tended to use considerably simplified models such as the Reynolds equation (see, e.g., Bayada & Chambat[5],

---

*SeLasCo GmbH, Waldstückerring 44, 76756 Bellheim, Germany
[†]Institute of Applied Mathematics, Heidelberg University, Im Neuenheimer Feld 294, 69120 Heidelberg, Germany (`stefan.frei@iwr.uni-heidelberg.de`)

Jubault et al.[27] as well as Hart et al.[21] including concepts of goal-oriented error estimation). In the derivation of the Reynolds equation the viscosity is assumed to be constant. However, when dealing with high pressures the viscosity strongly depends on the pressure and cannot be assumed as constant anymore. It is emphasized in Rajagopal & Szeri[33] that including a pressure-dependent viscosity into the Reynolds equation afterwards makes its whole derivation inconsistent. The full system of the Navier-Stokes equations have been used in Almqvist & Larsson[1] while treating the deformation of the fluid's domain with a simple ad hoc model, however. Furthermore, a splitting-type algorithm has been employed, which is computationally expensive. In this article, we will use the full Navier-Stokes equation within a fully monolithic formulation in order to guarantee robustness up to high-speed rotations. For the pressure-viscosity relation, we use the Barus law, which is expected to provide a reasonable approximation at least within a certain realistic pressure range.

In reality the viscosity is not only depending on pressure but also on temperature. The large local variations in pressure will cause essential changes in temperature. Therefore, we propose to include temperature as an additional variable within the fluid domain and augment the system by an energy conservation equation. It has already been noted in Almqvist & Larsson[1] that including thermal effects may lead to improved stability properties of the full system.

Our solution approach is based on Knauf[28] where, for the first time, a complete fluid-structure interaction formulation has been applied to elasto-hydrodynamic problems. Independently, in Bruyere et al.[12] a similar approach has been proposed also including fluid-structure interactions. In both these works, however, the numerical results presented were obtained for numerically "nice" situations, i.e., within a moderate range of rotational speed and for high temperatures. In this article, we will give details on the numerical techniques, which are necessary to handle more involved situations present in practical applications.

Furthermore, in contrast to Bruyere et al.[12], we are not only interested in the simulation of the system in the contact region between ball and race but also on the inflow and outflow regions of the lubricant. Hence, we will not assume the outer boundary of the lubricant to be fixed but consider it as an additional variable within a free boundary problem. For including this aspect into our simulations, we again propose the ALE approach. The ALE method has already been applied in various publications to free surface problems. The evolution of the free boundary is hereby treated either explicitly as in Souli & Zolesio[34] and Dettmer & Perić[13] or semi-implicitly as in Bänsch[4]. This imposes severe restrictions on the time-step depending on the spatial discretization that are particularly inconvenient in elastohydrodynamic simulations where the computational domains are typically highly anistropic. In this article, we propose a novel, fully-implicit treatment of the free boundary by means of Nitsche's method (Nitsche[31]). In the situation of bearings it turns out that accurately capturing the position of the fluid boundary is essential for the stability of the whole numerical algorithm. However, once the position of this boundary is determined with sufficient accuracy, it has only little impact on the local balance of forces, such that it is possible to separate these two aspects of the problem.

The complete system used here for describing elastohydrodynamic lubrication in ball bearings poses a variety of challenges for numerical computations. First, the geometry of the fluid domain Ω_f is highly anisotropic. While the oil film height lies typically within a range of nano- to micrometers, the radius of a ball is at least some millimeters. This enforces the use of highly aniso-tropic cells in an economical finite element discretization. Second, the pressure develops a large peak near the center of contact between ball and race leading to extreme variations in pressure within the lubricant. To deal with these high pressure values, "artificial" compressibility has been used in many publications (see, e.g., Franta et al.[15]). Indeed for pressure values larger than 0.1 GPa the assumption of incompressibility is not fully justified anymore. Therefore, we consider it more natural to incorporate real "physical" compressibility into the model. It turns out that including a compressibility term in the continuity equation leads to a significant reduction of

the pressure peak and thereby to a stabilization of the numerical approximation. Furthermore, we will make use of homotopy methods in order to cope with the strongly coupled nonlinearities in our monolithic formulation.

By this combination of robust methods for modelling, discretization and solution, we are for the first time able to present detailed simulations of the lubricant film dynamics in ball bearings in the regime of relevant technical parameters with rotational speeds up to 6 000 rpm and realistic temperature environments. Former approaches were either based on simplified models or considered alleviated configurations by using small rotational speeds. Because of the complexity of the resulting numerical algorithms, we restrict ourselves to simulations of the two dimensional version of the model. The extension to three dimensions merely entails technical difficulties, e.g., in mesh generation and, of course, with respect to computing time.

The outline of this article is as follows. First, in Section 2, we derive the continuum mechanical models used for the lubricant and the structure. We will describe our monolithic treatment of the fluid-structure interaction and formulate the Barus-Vogel law used for the pressure-temperature-viscosity relation. Further, we introduce our compressibility model and describe our geometric modeling ansatz and our treatment of preloading. In Section 3, we describe the spatial discretization, the numerical stabilization and the numerical algorithm we use. In Section 4, we derive a fully-implicit scheme for following the evolution of the free boundary and compare it to the results in previous works using explicit or semi-implicit algorithms. We validate our approach by means of a benchmark problem from Bänsch[4] and show results obtained for a ball bearing configuration. Section 5 is devoted to numerical results including fluid-structure interaction on realistic ball bearing geometries. First, we compare our results to those obtained from the Hamrock-Dowson formula (Hamrock et al.[18]) and study the convergence of the method under mesh refinement. Then, we investigate the effect of "artificial" compressibility and compare it to that observed by using real "physical" compressibility. Finally, we show some physical quantities, which are of particular importance for understanding elastohydrodynamic effects in ball bearings. This includes results of a comparison of loss torque values with those obtained from models developed by our industrial partner Rockwell Collins Germany GmbH.

2 Models

In this section, we describe the important physical effects included in our lubrication model. The domain of interest for modeling and simulation is depicted in Figure 1. In this work, we restrict ourselves to study one ball of the bearing neglecting possible interactions with neighbouring balls which might be subject to future work. We consider a cut plane through the midpoint of a ball which includes the contact region between ball and race. The latter depends on the direction (angle α) in which a prescribed preloading force is acting (cf. Sections 2.5 and 2.6). The ball rotates around the horizontal axis with angular velocity ω.

One ball within a ball bearing is completely surrounded by a thin oil film. At the upper and lower side the ball is nearly in contact with the inner and outer race, respectively, separated only by the lubricant. At the left and right-hand side, the lubricant has a free surface, outside of it being either atmospheric air or vacuum in applications in aeronautics.

2.1 Equations

For modeling fluid flow, we use the full Navier-Stokes equations for a generalized Newtonian fluid with pressure- and temperature-dependent viscosity. These equations are given in Eulerian
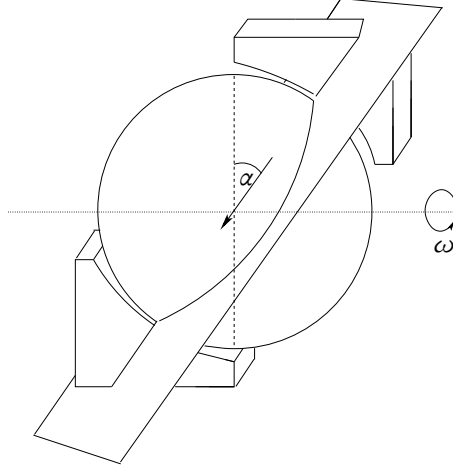
Figure 1. Cut plane through the contact regions for a 2d simulation for a contact angle α and rotational velocity ω

coordinates by

$$-\nabla \cdot \sigma_f + \rho_f v_f \cdot \nabla v_f = 0 \quad \text{in} \, \Omega_f, \tag{1a}$$

$$\nabla \cdot (\rho_f v_f) = 0 \quad \text{in} \, \Omega_f. \tag{1b}$$

Here, v_f denotes the fluid velocity, ρ_f the fluid density and Ω_f the domain occupied by the lubricant film, which will depend on the deformation of ball and race. The stress tensor σ_f consists of a pressure and a shear part,

$$\sigma_f = -p_f I + \mu(p_f, \theta_f)(\nabla v_f + \nabla v_f^T). \tag{2}$$

The fluid viscosity μ depends on the pressure p_f and the temperature θ_f. In order to prescribe this relationship, different models have been suggested in the literature (see, e.g., Hamrock et al. [19], Jubault et al. [27]). One of the most common models is the Barus' law. Assuming for a moment constant temperature, $\theta_f \equiv \theta_0$, the pressure-viscosity relationship reads

$$\mu(p_f) = \mu_0 e^{\alpha_0 p_f}. \tag{3}$$

The constants μ_0 and α_0 depend on the temperature and will be given later. Barus' law is known to yield a reasonable approximation within a moderate pressure range, but may fail at high values near 1 GPa (see, e.g., Ohno et al. [32]). Hence, we will include a cutoff-value for the pressure-viscosity relationship,

$$\mu(p_f) = \min\{\mu_0 e^{\alpha_0 p_f}, \mu_{\text{cutoff}}\}. \tag{4}$$

While the expected deformation of the structure domain $\hat{\Omega}_s$ (ball and race) is relatively large in comparison to the fluid film thickness, its deformation will in general be rather small in comparison to its size. Therefore, we can use the linear St. Venant-Kirchhoff material law for the structure. Let $\hat{u}_s$ denote the structure's deformation, $\hat{T}_s(\hat{x}) = \hat{x} + \hat{u}_s(\hat{x})$ the transformation map, $\hat{F}_s = I + \hat{\nabla} \hat{u}_s$ its Jacobian and $\hat{J}_s = \det(\hat{F}_s)$ the Jacobian determinant. We use the "hat" notation in order to indicate Lagrangian quantities. Defining the strain tensor $\hat{E}_s$ and the first Piola-Kirchhoff stress
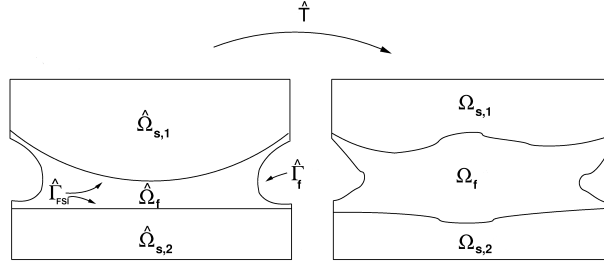
Figure 2. Scheme of the ALE transformation for a part of a ball bearing geometry

tensor $\hat{P}_s$ by

$$\hat{E}_s = \tfrac{1}{2}(\hat{F}_s^T \hat{F}_s - I), \tag{5}$$

$$\hat{P}_s = \hat{F}_s(\lambda(\mathrm{tr}(\hat{E}_s)) + 2\mu\hat{E}_s) =: \hat{J}_s \hat{\sigma}_s \hat{F}_s^{-T}, \tag{6}$$

the resulting structure equations read in Lagrangian coordinates as follows:

$$\begin{aligned}
-\hat{\nabla} \cdot \hat{P}_s &= 0 \quad \text{in}\,\hat{\Omega}_s, \\
\hat{P}_s \cdot n &= g_f \quad \text{on}\,\hat{\Gamma}_{\mathrm{FSI}}.
\end{aligned} \tag{7}$$

Here, $\hat{\Gamma}_{\mathrm{FSI}}$ refers to the interface between fluid and structure. By g_f, we denote the boundary force the fluid exerts on the structure. In (6), we also introduced the Cauchy stress tensor $\hat{\sigma}_s$ for later purposes.

2.2 Fluid-structure interaction

As explained in the introduction, one of the most crucial aspects in modeling lubrication flow in ball bearings is the interaction of the lubricant with the surrounding structures, typically steel in ball and race. When considering high rotational speeds (e.g., > 1000 rounds per minute), high pressure values arise in the contact region between ball and race. This leads to considerable deformations in relation to the lubricant film thickness. On the other hand the fluid's pressure profile is quite sensitive to changes in the shape of the fluid's domain. Eventually, the system reaches a state fulfilling a balance of forces between fluid and structure. In view of its importance, we treat this interaction in an implicit way within a monolithic ALE approach. The monolithic ALE approach is known to yield a robust numerical scheme, which allows for large time steps. Furthermore, having our particular application in mind, the system is expected to reach a stationary limit. This limit can be calculated directly using a monolithic scheme while partitioned schemes would require an expensive time stepping to reach the stationary limit.

The idea behind the ALE approach is to formulate the fluid equations on a fixed reference domain $\hat{\Omega}_f$ via a transformation onto the "physical" domain Ω_f,

$$\hat{T}_f : \hat{\Omega}_f \mapsto \Omega_f, \quad \hat{T}_f(\hat{x}) = \hat{x} + \hat{u}_f(\hat{x}). \tag{8}$$

The scheme of the ALE transformation for a part of a ball bearing geometry is shown in Figure 2. Here, $\hat{\Omega}_{s,1}$ stands for one ball in a bearing geometry and $\hat{\Omega}_{s,2}$ for the corresponding race in the reference state, which is before deformation. By $\hat{\Omega}_f$, we denote the domain occupied by the lubricant in the reference state. The treatment of the free boundary Γ_f will be the subject of

Section 4. The union of the interfaces between $\hat{\Omega}_f$ and $\hat{\Omega}_{s,i}$ is denoted by $\hat{\Gamma}_{FSI}$. Its transformation is given by the solid's deformation

$$\hat{T}_f|_{\hat{\Gamma}_{\text{FSI}}} = id + \hat{u}_s. \tag{9}$$

Inside the domain $\hat{\Omega}_f$, we can use an arbitrary deformation. In the following, we will use a harmonic extension inside $\hat{\Omega}_f$, but other extensions are possible as well (see, e.g., Dunne et al. [14]). Similar as for the structure part, we introduce the flow deformation gradient $\hat{F}_f$ and its determinant $\hat{J}_f$ by

$$\hat{F}_f = I + \hat{\nabla}\hat{u}_f, \quad \hat{J}_f = \det \hat{F}_f. \tag{10}$$

Then, the fluid equations in ALE coordinates read as follows:

$$\hat{J}_f \rho_f \hat{F}^{-1}\hat{v}_f \cdot \hat{\nabla}\hat{v}_f - \hat{\nabla}\cdot\left(\hat{J}_f \hat{\sigma}_f \hat{F}^{-T}\right) = 0 \quad \text{in}\,\hat{\Omega}_f, \tag{11a}$$

$$\hat{\nabla}\cdot(\hat{J}_f \rho_f \hat{F}_f^{-1}\hat{v}_f) = 0 \quad \text{in}\,\hat{\Omega}_f, \tag{11b}$$

where

$$\hat{\sigma}_f = -\hat{p}_f I + \mu_f(\hat{p}_f)\left(\hat{\nabla}\hat{v}_f \hat{F}_f^{-1} + \hat{F}_f^{-T}\hat{\nabla}\hat{v}_f^T\right). \tag{12}$$

The coupling conditions between fluid and solid are given by

$$\hat{v}_f = \hat{v}_s,$$
$$\hat{J}_s \hat{\sigma}_s \hat{F}_s^{-T}\hat{n} = \hat{J}_f \hat{\sigma}_f \hat{F}_f^{-T}\hat{n} \,(= g_f) \quad \text{on}\,\hat{\Gamma}_{\text{FSI}}. \tag{13}$$

Both conditions will be incorporated implicitly into a monolithic variational formulation, the first one strongly by requiring continuity of the trial functions for the velocity, the second one weakly as a natural boundary condition. For details on the derivation of the ALE formulation, we refer to Dunne et al. [14]. For better readability, we define global functions v by $v_{|\Omega_f} := v_f$ and $v_{|\Omega_s} := v_s$ and similarly for the other variables. Altogether the monolithic weak formulation reads as follows:
Find $(\hat{u}, \hat{v}, \hat{p}) \in \left((u^D + U) \times (v^D + U) \times X\right)$, *such that*

$$\begin{aligned}
&(\hat{J}\rho\hat{F}^{-1}\hat{v}\cdot\hat{\nabla}\hat{v}, \phi_v)_{\hat{\Omega}_f} + (\hat{J}\hat{\sigma}_f\hat{F}^{-T}, \hat{\nabla}\phi_v)_{\hat{\Omega}_f} \\
&+ (\hat{J}\rho\hat{F}^{-1}\hat{v}, \hat{\nabla}\phi_p)_{\hat{\Omega}_f} + \alpha_u(\hat{\nabla}\hat{u}, \hat{\nabla}\phi_u)_{\hat{\Omega}_f} \\
&+ (\hat{J}\rho\hat{\sigma}_s\hat{F}^{-T}, \hat{\nabla}\phi_v)_{\hat{\Omega}_s} \\
&= 0 \quad \forall \left((\phi_u, \phi_v, \phi_p) \in (U \times U \times X)\right)
\end{aligned} \tag{14}$$

2.3 Thermal model

The large variations in pressure within the lubricant lead to local temperature effects such that the assumption of a constant temperature within the lubricant is not justified anymore. On the other hand, viscosity is quite sensitive with respect to temperature. Hence, we will treat the temperature θ_f as an additional variable within the fluid. The constitutive (stationary) energy conservation equation reads

$$c_p \rho_f v_f \nabla\theta_f - \sigma_f : \nabla v_f - \nabla\cdot(\kappa_c \nabla\theta_f) = 0 \quad \text{in}\,\Omega_f, \tag{15}$$

where c_p is the heat capacity and κ_c the (known) heat conductivity of the lubricant. For modeling the temperature-viscosity relation, we use the so-called "Vogel equation". The combined Barus-Vogel law for the pressure-temperature-viscosity relation reads

$$\mu(p_f, \theta_f) = e^{\alpha(\theta_f)p_f} \left(e^{A/\theta_f^m} - C \right), \tag{16}$$

with constants C, m and A corresponding to the lubricant under consideration.

Remark 2.1. *In our numerical simulations, it turned out that including thermal effects had a positive effect on numerical stability in the case of high-speed rotations. The reason for this is the following: An increase in speed leads to an even higher pressure peak in the area of contact. Due to Barus' law this affects the exponential viscosity profile which causes severe difficulties in the numerical simulation. However, when including temperature dependence, the increase of frictional forces caused by the high velocity increases temperature as well. This effect corresponds to the second term in our energy model (15). An increase in temperature, on the other hand, would lead to a decay in viscosity if pressure remained fixed. Thus, the temperature effect limits the increase in viscosity caused by pressure. Altogether, the account for variability of temperature leads to a smoothening of the viscosity profile which makes simulations at high rotational speeds possible at all. This effect has already been found in Almqvist & Larsson[1] for rather moderate speeds < 1m/s.*

For our application in mind, there might occur temperature differences up to several degrees Kelvin between race and ball. The assumption of continuity of temperature between oil and steel would be too strong and unrealistic. Hence, we suggest Robin boundary conditions on the fluid-structure interface

$$\Gamma_{\mathrm{FSI}} = \Gamma_{\mathrm{ball}} \cup \Gamma_{\mathrm{race}}. \tag{17}$$

Denoting the free boundary of the lubricant by Γ_f, the boundary conditions we use read as follows:

$$\begin{aligned} \partial_n \theta &= 0 \quad \text{on } \Gamma_f \\ \kappa_c \partial_n \theta &= -\alpha_{\mathrm{s/o}}(\theta - \theta_{\mathrm{ball}}) \quad \text{on } \Gamma_{\mathrm{ball}} \\ \kappa_c \partial_n \theta &= -\alpha_{\mathrm{s/o}}(\theta - \theta_{\mathrm{race}}) \quad \text{on } \Gamma_{\mathrm{race}} \end{aligned} \tag{18}$$

Here, we use the heat transfer coefficient $\alpha_{\mathrm{s/o}}$ given by

$$\alpha_{\mathrm{s/o}} \approx \kappa_c/\delta, \tag{19}$$

where δ denotes the height of the thermal boundary layer. While local thermal effects play an important role in the fluid, the solid's material parameters are much less sensitive to temperature. In the numerical simulations conducted for this paper, the solid's temparature was known from experiments and we could set them as input parameters θ_{ball} and θ_{race} for the fluid's thermal equation. In principle, it would also be possible to solve an additional energy equation in the solid domain. One has to take care of spurious feedback effects to the fluid's temperature, however.

2.4 Compressibility

One of the most critical aspects to be considered in deriving a robust numerical algorithm for ball bearing simulations is the treatment of the pressure peak arising near the center of contact. In addition to the smoothing effect of including temperature described above, we have to develop a strategy for controlling the pressure. In the literature, the use of artificial compressibility is

mostly the method of choice (see, e.g., Franta et al. [15] for a theoretical analysis). This consists in weakening the incompressibility constraint (1b) by adding a small diffusive term,

$$\nabla \cdot (\rho_f v_f) - \epsilon \Delta p_f = 0. \tag{20}$$

The parameter ϵ is not a physical one, but is rather introduced for numerical stability. Typically, one chooses $\epsilon = \mathcal{O}(h_T^2)$ where h_T is a local mesh size parameter (e.g., the diameter of a mesh cell T). Due to the geometry in ball bearing applications, however, we have to use rather small cells in the area of contact where the pressure peak arises. Hence, the meshsize-based regularization strategy may fail and simulation break down for numerically involved situations. In the numerical simulations conducted for this paper it turned out that we had to fix ϵ to a rather moderate value independent of the local h_T in order to ensure our nonlinear iteration to converge with reasonable speed. This however leads to unphysical perturbations in the pressure and velocity profile (see Section 5). Hence, we follow another more natural way of dealing with large pressures by considering a pressure-density relation of the form

$$\rho_f(p_f) = \rho_0 e^{p_f/K} \tag{21}$$

with the lubricant specific bulk modulus K. Using this relation, the continuity equation takes the form

$$\rho_0 e^{p_f/K} \nabla \cdot v_f + \frac{\rho_0}{K} e^{p_f/K} v_f \cdot \nabla p_f = 0 \quad \text{in} \, \Omega_f. \tag{22}$$

Though this introduces another nonlinearity into our variational formulation, our numerical results indicate that it leads to even better stability properties than the artificial compressibility ansatz without perturbing the pressure profile in an unphysical way.

2.5 Treatment of preloading

In reality, ball bearings are preloaded, which means that the ball is pressed against the race by a spring-like structure with defined force. This force changes the initial geometry of the structure. It leads to a flattening of the ball near the center of contact and causes high pressure between ball and race.

In order to incorporate preloading, we will make use of the so-called "Hertzian" contact theory (Hertz [22]). This theory is widely used in the literature for ball bearings. It describes pressure profiles and resulting deformations analytically for two simple-shaped bodies pressed against each other. As the force acting on a ball is in general not orthogonal to the race, the contact surface will be elliptic with semi-axis a and b. Denoting the center of this ellipse by (x_0, y_0) the resulting pressure profile for a prescribed force F is given by

$$p_0(x, y) = p_{\max} \sqrt{1 - \left(\frac{x - x_0}{a}\right)^2 - \left(\frac{y - y_0}{b}\right)^2},$$
$$p_{\max} = \frac{3}{2} \frac{F}{\pi a b}. \tag{23}$$

The semi-axis a and b depend on the force F themselves and can be calculated by the Hertzian theory (see, e.g., Hamrock et al. [19]).

We assume a splitting of the total pressure

$$p = p_0 + p_f$$

into a part p_0 arising from the preloading force and a hydrodynamic part p_f which is a reasonable approximation for small preloading. Instead of (13), the balance of forces is then given by

$$\hat{J}_s \hat{\sigma}_s \hat{F}_s^{-T} \hat{n} = \hat{J}_f \hat{\sigma}_f \hat{F}_f^{-T} \hat{n} - \hat{J}_f p_0 \hat{n}. \tag{24}$$

Clearly, this strategy only works for relatively small preloading. For higher preloading, we have to incorporate the initial deformation directly by modifying the initial geometry and solving for the total pressure p. An entirely physical formulation of contact forces would require the simulation of a contact problem leading to a variational inequality. This approach is however beyond the scope of the present article.

2.6 Geometric Modeling

In the present work, we consider a cut plane through the middle of a ball which includes the major semiaxis of the Herzian contact ellipsoid neglecting the third dimension normal to this plane (see Figure 1).

Now, the two dimensional Hertzian pressure profile on Γ_{FSI} is given by

$$p_0(x) = p_{\max} \sqrt{1 - \left(\frac{x - x_0}{a} \right)^2}$$

and the minimum of the film thickness will be taken within this plane. All effects perpendicular to the cut plane can only be integrated by a projection onto the plane. In our case, the radial preloading leads to different boundary conditions for the velocity at the fluid-structure interface. Furthermore, the amount of lubricant that is present, is determined by the initial geometry which thus influences quantities like the fluid film thickness, etc.

3 Numerical aspects

3.1 Discretization

For the discretization of the Navier-Stokes- and the elasticity equations, there is available a variety of different finite element methods. First of all, we may choose between "inf-sup stable" and stabilized elements. "Equal-order" finite elements, e.g., $Q_1 Q_1$-elements for velocity and pressure, are easy to implement and very efficient algebraic solvers can be constructed. However, they do not fulfill the *inf-sup-stability condition* and therefore have to be stabilized (see Tezduyar et al. [35] or Girault & Raviart [16] for a general discussion on the discretization of incompressible flows). For this stabilization, we can choose between the *Local Projection Stabilization (LPS)* (see Becker & Braack [6]) or the *Galerkin Least-Squares Stabilization (GLS)* (see Hughes et al. [26]). Stabilization on highly anistropic meshes is not straightforward, however. The standard stabilization techniques are not robust with respect to the cell aspect ratio. Therefore, we have to take into account the local anistropy within the stabilization terms (see Braack [9] for LPS and Apel et al. [3] for GLS). The type of stabilization is crucial when considering pressure-dependent viscosities fulfilling for instance Barus' equation. When employing GLS, we observed unphysical boundary layers in the pressure at Neumann-type boundaries, which is especially a problem for free boundary value problems. Hence, for the numerical results shown in Section 4, we have used anisotropic LPS.

The LPS technique is based on local projection of the pressure onto a coarser grid. In two dimensions typically four cells of a triangulation $\mathcal{T}_h$ are combined to form a patch $\mathcal{P} \in \mathcal{T}_{2h}$. We
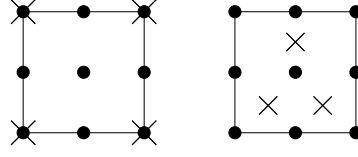
Figure 3. Arrangement of the velocity • and pressure × degrees of freedom for the inf-sup stable Q_2Q_1 Taylor-Hood and $Q_2P_1^{\text{disc}}$ element.

define the projection π_h as the L^2-projection into the space of patchwise constant functions

$$\pi_h(q) := \frac{1}{|\mathscr{P}|}\int_{\mathscr{P}} q\,dx. \tag{25}$$

Then, the operator

$$\kappa_h = id - \pi_h, \tag{26}$$

with id being the identity, is used as fluctuation filter for stabilization. Robust stabilization, independent of the cell aspect ratio (in x- and y coordinate direction), is now ensured by adding the term

$$
\begin{aligned}
s_{\text{lps}} := &\left(\alpha_x\partial_x(\kappa_h p),\partial_x(\kappa_h\phi^p)\right)\\
&+ \left(\alpha_y\partial_y(\kappa_h p),\partial_x(\kappa_h\phi^p)\right)\\
&+ \left(\delta_x v_1\partial_x(\kappa_h v),v_1\partial_x(\kappa_h\phi^v)\right)\\
&+ \left(\delta_y v_2\partial_y(\kappa_h v),v_2\partial_y(\kappa_h\phi^v)\right)
\end{aligned}
\tag{27}
$$

in the variational formulation. Defining a local anisotropic variant of the Peclét number on a cell T by

$$\text{Pe}_T := \frac{\|v\|_{T,\infty}\min\left(h_T^x,h_T^y\right)}{\mu}, \tag{28}$$

the cell parameters $\delta_x,\delta_y,\alpha_x,\alpha_y$ are given by

$$
\begin{aligned}
\alpha_x|_T &= \alpha_0\frac{(h_T^x)^2}{\mu}\min\left(1,Pe_T^{-1}\right),\\
\delta_x|_T &= \|v\|_{T,\infty}^2\alpha_x|_T,\\
\alpha_y|_T &= \alpha_0\frac{(h_T^y)^2}{\mu}\min\left(1,Pe_T^{-1}\right),\\
\delta_y|_T &= \|v\|_{T,\infty}^2\alpha_y|_T.
\end{aligned}
\tag{29}
$$

This choice of parameters leads to a discretization that fulfills an *inf-sup stability condition* independently of the cell aspect ratio, while preserving the optimal order of convergence (Braack[9]).

As alternative to the equal-order finite element, we will also consider the inf-sup stable Q_2Q_1- and $Q_2P_1^{\text{disc}}$-Taylor-Hood elements (see Girault & Raviart[16]). Figure 3 illustrates the arrangement of the degrees of freedom for both elements. In both free surface and fluid-structure-interaction problems, local mass conservation plays an important role, which requires the use of cellwise discontinuous pressure trial functions. Furthermore, for fluid-structure interaction it appears advantageous to have a discontinuous pressure along the interface. Both of these requirements favour the $Q_2P_1^{\text{disc}}$- element, which has been used for the simulation of fluid-structure interaction in Section 5. For discretization of the temperature and the structure's deformation, we will always consider the velocity element.

3.2   Stabilization of Temperature

The energy equation (15) written in terms of temperature takes the following form

$$c_p \rho_f v_f \cdot \nabla \theta_f - \nabla \cdot (\kappa_c \nabla \theta_f) = F(p_f, v_f) \quad \text{in } \Omega_f \tag{30}$$

In lubrication flow this equation is usually strongly transport dominated as $c_p \rho_f \gg \kappa_c$. Hence, we have to include a cellwise stabilization term into the variational equation. Here, we will make use of the streamline-diffusion method (Hughes & Brooks[25]) by adding the term

$$\sum_{T \in \mathcal{T}_h} \left(c_p \rho_f \delta_0 v_f \cdot \nabla \theta_f, v_f \cdot \nabla \phi \right)_T, \tag{31}$$

where

$$\delta_0 = \min \left\{ h_T, \frac{c_p \rho_f h_T^2}{\kappa_c} \right\}, \quad h_T = \text{diam}(T). \tag{32}$$

3.3   Numerical algorithm

In order to get a robust algorithm for high-speed situations, we use a discretization scheme which is based on a fully-coupled monolithic model formulation combining (14) and (15). We emphasize that this also includes the deformation of the domain due to the fluid-structure interaction. This is in contrast to Almqvist & Larsson[1] where the aspects fluid dynamics, thermal effects and deformation appear separated within a partitioned solution approach. In addition to its robustness, the monolithic approach allows for a direct calculation of stationary states, which are of primary interest in this paper. To deal with the nonlinearities, we use certain variants of the Newton method.

The simulation of high-speed situations requires good initial values for the Newton iteration. This is achieved by the use of homotopy techniques. Starting from a small rotational velocity v^D, we increase the velocity gradually taking in each step the solution from the previous step as initial value. This is done in a self-adaptive way, i.e., we try to increase the speed increment as far as possible as long as Newton convergence is achieved within a reasonable number of iterations.

An important ingredient for the fluid-structure interaction calculation is a suitable initial geometry which depends on free surfaces in the fluid domain. In our numerical simulations, it turned out that once a suitable initial geometry is known, the free surface conditions play a minor role for the overall dynamics. Furthermore, for simulations at high rotational velocities, it is difficult to combine both the free boundary problem and the fluid-structure interaction in one computation. Hence, we decided to split both problems calculating the position of the free boundary in advance and solving the FSI problem afterwards with fixed outer boundaries. For the latter problem, we solve directly for a stationary state using Newton's method.

4   Numerical treatment of the free surface problem

In this section, we introduce a discretization scheme for free surface problems including a fully implicit treatment of the free boundary movement. As already mentioned above, in ball bearing applications the outer boundary of the lubricant is unknown. In our two dimensional simulation domain we have to include two free boundary parts Γ_f at the left and right meniscus (cf. Figure 2). To study the influence of the free boundary parts perpendicular to the running direction, we would need a three dimensional simulation. This is however beyond the scope of the present paper.

A similar free-boundary value problem has been considered, e.g., in Bänsch[4]. Let the velocity of the evolution of the free boundary be denoted by V_n, which will become an unknown in our approximation later on. Further, let $\Omega_f(t)$ denote the time-dependent domain with boundary $\Gamma(t) = \Gamma_f(t) \cup \Gamma_D$ consisting of a free boundary component $\Gamma_f(t)$ and a fixed component Γ_D, at which for simplicity, we impose Dirichlet boundary conditions. Then, the system under consideration reads as follows:

$$\rho \partial_t v + \rho(v \cdot \nabla)v - \nabla \cdot \sigma(p, v) = \rho f, \quad \text{in } \Omega_f(t) \tag{33}$$

$$\nabla \cdot v = 0, \quad \text{in } \Omega_f(t) \tag{34}$$

$$\sigma(p, v) = -pI + \mu(\nabla v + (\nabla v)^T), \tag{35}$$

$$v(\cdot, 0) = v_0, \quad \Omega_f(0) = \Omega_0, \tag{36}$$

$$V_n = (n \cdot v)n, \quad \text{on } \Gamma_f(t), \tag{37}$$

$$v = 0, \quad \text{on } \Gamma_D, \tag{38}$$

$$t \cdot \sigma \cdot n = 0, \quad \text{on } \Gamma_f(t), \tag{39}$$

$$n \cdot \sigma \cdot n = \gamma \kappa n, \quad \text{on } \Gamma_f(t). \tag{40}$$

Here, γ is a surface tension parameter and κ denotes the curvature of the free boundary. As in Section 2.2, we will make use of an *Arbitrary Lagrangian Eulerian (ALE)* method in order to incorporate the movement of the domain $\Omega_f(t)$ into a variational formulation. We will use the notation introduced in Section 2.2, e.g.,

$$\hat{T}_f : \hat{\Omega}_f \times [0, T] \mapsto \Omega_f(t), \quad \hat{T}_f(\hat{x}, t) = \hat{x} + \hat{u}(\hat{x})(t).$$

The boundary condition (37) reads in ALE coordinates

$$\partial_t \hat{u} = \left(\frac{F^{-T}\hat{n}}{||F^{-T}\hat{n}||} \cdot \hat{v} \right) \frac{F^{-T}\hat{n}}{||F^{-T}\hat{n}||}, \quad \text{on} \quad \Gamma_f(0). \tag{41}$$

We note that here the velocity V_n of the evolution of the free boundary is incorporated by means of the additional unknown $\hat{u}$.

4.1 Time-stepping schemes

In order to derive a fully implicit algorithm and for comparison, we start with a short review of related algorithms used in the literature. The ALE method has been used in Souli & Zolesio[34] and Dettmer & Perić[13] within time-stepping schemes that include the movement of the boundary explicitly, however.

Problem 4.1 (Semi-implicit formulation of the free boundary value problem). *Let the time interval* $[0, T]$ *be divided into* m *equidistant time-steps of size* Δt. *For* $n \in \{0, ..., m-1\}$ *proceed as follows:*

1. *Find* $v^n := v(t^n)$, $u^n := u(t^n) \in V$, $p^n := p(t^n) \in X$, *such that*

$$\Delta t^{-1}(\hat{J}^{n+1}\rho\hat{v}^{n+1} - \hat{J}^n\rho v^n, \phi) + \theta(\hat{J}^{n+1}\rho(\hat{v}^{n+1} - \partial_t \hat{u}^{n+1}) \cdot \hat{\nabla}\hat{v}^{n+1}, \phi)$$

$$+ \theta(\hat{J}\hat{\sigma}(\hat{p}^{n+1}, \hat{v}^{n+1})\hat{F}^{-T,n+1}, \hat{\nabla}\phi) + (1-\theta)(\hat{J}^n\rho(\hat{v}^n - \partial_t \hat{u}^n) \cdot \hat{\nabla}\hat{v}^n, \phi)$$

$$+ (1-\theta)(\hat{J}^n\hat{\sigma}(\hat{p}^n, \hat{v}^n)\hat{F}^{-T,n}, \hat{\nabla}\phi) \tag{42}$$

$$= \theta(\hat{J}^{n+1}\rho f^{n+1}, \phi) + (1-\theta)(\hat{J}^n\rho f^n, \phi) + \gamma < \kappa n, \phi >_{\Gamma_f} \tag{43}$$

$$(\hat{\nabla} \cdot (\hat{J}^{n+1}\hat{v}^{n+1}\hat{F}^{-1,n}), \chi) = 0, \tag{44}$$

$$\hat{u}^{n+1}, \nabla\psi) = 0, \tag{45}$$

for all $\phi, \psi \in V$, $\chi \in X$.

2. *Update the position of the free boundary*

$$\hat{u}^{n+1} = \hat{u}^n + \Delta t (n^n \cdot \hat{v}^n) n^n, \quad \text{on} \quad \hat{\Gamma}. \tag{46}$$

Here, $\theta = 1$ corresponds to the backward Euler scheme, while $\theta = 0.5$ yields the Crank-Nicolson scheme (trapezoidal rule). For better readability, we have used the notation

$$n = \frac{\hat{F}^{-T}\hat{n}}{\|\hat{F}^{-T}\hat{n}\|}. \tag{47}$$

The curvature term (43) can be evaluated numerically using the Laplace-Beltrami operator. When including the curvature terms explicitly, we set, for $t \in [t_n, t_{n+1}]$,

$$
\begin{aligned}
< \kappa n, \phi >_{\Gamma_f(t)} &\approx \int_{\Gamma_f^n} \kappa n \phi \, ds \\
&= \int_{\Gamma_f^n} \overline{\Delta} id|_{\Gamma_f^n} \phi \, ds \\
&= -\int_{\Gamma_f^n} \overline{\nabla} id|_{\Gamma_f^n} \overline{\nabla} \phi \, ds.
\end{aligned} \tag{48}
$$

In ALE coordinates this can be evaluated by

$$
\begin{aligned}
\int_{\Gamma_f^n} \overline{\nabla} id|_{\Gamma_f^n} \overline{\nabla} \phi \, ds &= \int_{\hat{\Gamma}_f} \left(\hat{F}^{-1,n} \hat{\nabla} - n \hat{F}^{-1,n} \hat{\nabla} n \right) id_{\hat{\Gamma}_f} \\
&\quad \cdot \left(\hat{F}^{-1,n} \hat{\nabla} - n \hat{F}^{-1,n} \hat{\nabla} n \right) \phi \, \hat{J}^n \|\hat{F}^{-T,n} \hat{n}\| \, d\hat{s},
\end{aligned}
$$

using the transformed normal n given in (47). This time-discrete variational formulation is explicit with respect to the movement of the free boundary since its new position *only* depends on data of the last time-step. Such a discretization therefore can only be conditionally stable, i.e., the algorithm is stable only for sufficiently small time-steps. This means that temporal and spatial discretization are coupling, i.e., refinement of the spatial mesh may require progressively smaller time-steps. This effect has occurred in the various test simulations conducted for this paper and is also well known in the literature. A corresponding qualitative as well as quantitative analysis can be found in Brackbill et al.[11]. In order to ensure stability, the condition

$$\Delta t < \left(\frac{h^3 \rho}{\gamma} \right)^{1/2}. \tag{49}$$

has to be fulfilled. To overcome this restriction a semi-implicit treatment of the curvature terms has been proposed in Bänsch[4]. The new position of the free boundary at time t_{n+1} can be approximated by

$$\Gamma_f^{n+1} = \Gamma_f^n + \Delta t (v^{n+1} \cdot n^n) n^n. \tag{50}$$

Inserting (50) into the Laplace-Beltrami term in (48) the curvature term at the new time level can be evaluated semi-implicitly as follows:

$$
\begin{aligned}
< \kappa n, \phi >_{\Gamma_f(t)} &\approx \int_{\Gamma_f^n} \overline{\nabla} id|_{\Gamma_f^{n+1}} \overline{\nabla} \phi \\
&= \int_{\Gamma_f^n} \overline{\nabla} \left(id|_{\Gamma_f^n} + \Delta t (v^{n+1} \cdot n^n) n^n \right) \overline{\nabla} \phi.
\end{aligned} \tag{51}
$$

This semi-implicit treatment allows for much larger time-steps in practice. However, numerical experiments indicate that in fact the stability is still conditional and the problem has not completely been cured. This makes this approach delicate in the case of local mesh refinement and for the anisotropic grids we consider for elastohydrodynamic simulations.

For the following, we propose a fully implicit approach using a weak imposition of boundary values via Nitsche's method (Nitsche[31]). In the previous algorithms the equations are solved for fixed Dirichlet boundary values for the transformation $\hat{u}$ and are thus inherently explicit with respect to the treatment of the evolution of the free boundary. In order to impose the boundary condition

$$\partial_t u = (n \cdot v) n \quad \text{on } \Gamma_f^{n+1}, \tag{52}$$

Nitsche's method adds a penalty term to the variational formulation (43). A first-order approximation in time consists in adding the boundary term

$$\frac{\gamma_N}{h} \langle u^{n+1} - u^n - \Delta t (n^{n+1} \cdot v^{n+1}) n^{n+1}, \phi \rangle_{\Gamma_f^{n+1}}, \tag{53}$$

for γ_N sufficiently large. For a second-order approximation, we can use the term

$$\frac{\gamma_N}{h} \langle u^{n+1} - u^n - \tfrac{1}{2}\Delta t((n^{n+1} \cdot v^{n+1}) n^{n+1} \\ + (n^n \cdot v^n) n^n, \phi) \rangle_{\Gamma_f^{n+1}}. \tag{54}$$

The unknown boundary Γ_f^{n+1} is hereby included implicitly by means of the ALE deformation map. Due to the transformations the terms (53) and (54) contain strong nonlinearities. Different variants of Nitsche's method and strategies to choose γ_N with regard to stability issues have been proposed and analyzed in the literature (cf. Hansbo and Hansbo[20] or Annavaparu et al.[2]). Their application to the boundary condition (41) is not straightforward, however. For our numerical tests, we used a simple ad hoc strategy to determine γ_N.

Problem 4.2 (Fully implicit formulation of the free boundary value problem). *Let the interval* $[0, T]$ *be divided into* m *equidistant time-steps of size* Δt. *For* $n \in \{0, ..., m-1\}$ *find* $v^n := v(t^n)$, $u^n := u(t^n) \in V$ *and* $p^n := p(t^n) \in X$, *such that*

$$\Delta t^{-1}(\hat{J}^{n+1} \rho \hat{v}^{n+1} - \hat{J}^n \rho \hat{v}^n, \phi) + \theta(\hat{J}^{n+1} \rho(\hat{v}^{n+1} - \partial_t \hat{u}^{n+1}) \cdot \hat{\nabla} \hat{v}^{n+1}, \phi)$$
$$+ \theta(\hat{J} \hat{\sigma}(\hat{p}^{n+1}, \hat{v}^{n+1}) \hat{F}^{-T,n+1}, \hat{\nabla} \phi) + (1-\theta)(\hat{J}^n \rho(\hat{v}^n - \partial_t \hat{u}^n) \cdot \hat{\nabla} \hat{v}^n, \phi)$$
$$+ (1-\theta)(\hat{J} \hat{\sigma}(\hat{p}^n, \hat{v}^n) \hat{F}^{-T,n}, \hat{\nabla} \phi) + \gamma \langle \overline{\nabla} id_{\Gamma_f^{n+1}}, \overline{\nabla} \phi \rangle_{\Gamma_f^{n+1}}$$
$$- \frac{\gamma_N}{h} \langle u^{n+1} - u^n - \Delta t (\theta_N (n^{n+1} \cdot v^{n+1}) n^{n+1} + (1-\theta_N)(n^n \cdot v^n) n^n), \phi \rangle_{\Gamma_f^{n+1}}$$
$$= \theta(\hat{J} \rho f^{n+1}, \phi) + (1-\theta)(\hat{J} \rho f^n, \phi), \tag{55}$$
$$(\hat{\nabla} \cdot (\hat{J} \hat{v}^{n+1} \hat{F}^{-1,n}), \chi) = 0, \tag{56}$$
$$(\hat{\nabla} \hat{u}^{n+1}, \hat{\nabla} \psi) = 0, \tag{57}$$

for all $\phi, \psi \in V$, $\chi \in X$.

The above time-discrete formulation is stable for all choices of the time step size.

4.2 Numerical results for the free surface simulation

In order to compare and validate the numerical methods described above, we test them at the benchmark configuration given in Bänsch[4] known as "oscillating liquid drop". In two dimensions,
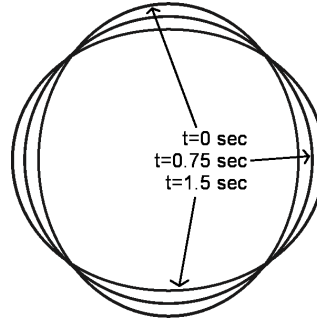
Figure 4. Oscillating bubble at four successive instances of time
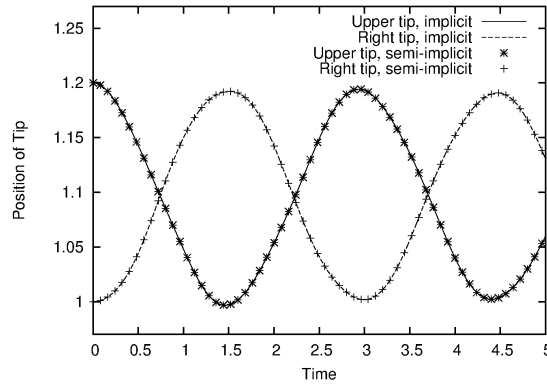

Figure 5. Time evolution of the position of the upper and right tip of the oscillating liquid drop for the fully implicit and semi-implicit scheme.

the computational domain consists of an ellipsoid with semi-axis $r_1 = 1$, $r_2 = 1.2$. The non-constant curvature of the boundary leads to oscillatory behaviour if viscous damping is small enough. The Reynolds number in this example is chosen as $\mathrm{Re} = 300$. According to the discussion in Section 3.1, we used the $Q_2 P_1^{\mathrm{disc}}$-, the $Q_2 Q_1$-Taylor-Hood element and the LPS-stabilized $Q_1 Q_1$-element for spatial discretization. The penalty parameter γ_N was chosen as 10^7. All our simulations were done using the Finite Element Toolkit G A S C O I G N E 3 D (Becker et al.[7]). For more details on the software implementation, we refer to Knauf[28].

In Figure 4, we depict the shape of the ellipsoid at different instances of time, $t = 0$ sec, $t = 0.75$ sec and $t = 1.5$ sec. Figure 5 shows the time evolution of the position of the upper and the right tip for the semi-implicit and the implicit scheme. The results of both schemes show very good agreement with the results given in Bänsch[4].

Next, we analyze our discretization schemes with respect to spatial and temporal accuracy. One of the most important quantities for free boundary applications is the error in mass conservation. In reality the mass remains constant and is given by $\overline{m} = \pi r_1 r_2$. The mass at time t_n in our numerical scheme is given by

$$m(t_n) = \int_{\hat{\Omega}} \hat{J}^n d\hat{x}. \tag{58}$$

In Figure 6, we show the change of volume in the course of time for the LPS-stabilized $Q_1 Q_1$- as well as the stable $Q_2 P_1^{\mathrm{disc}}$-element for three sucessively refined mesh with 337, 1313 and 5185 nodes. Computations using the $Q_2 Q_1$ element showed qualititavely and quantitively a very similar

a)

b)
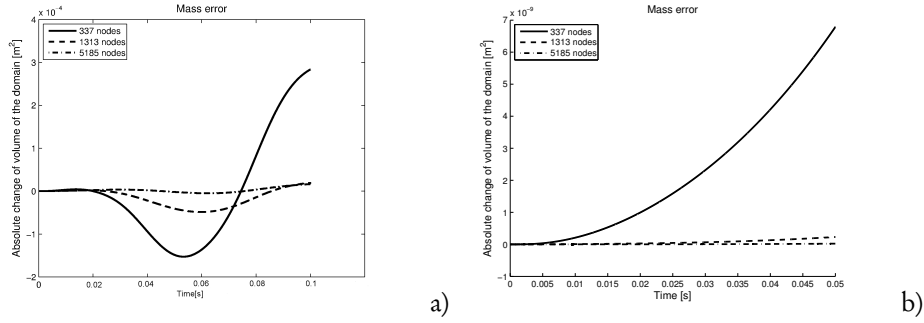
Figure 6. Mass error in the course of time for a) the LPS-stabilized Q_1Q_1-, and b) the $Q_2P_1^{\mathrm{disc}}$-element on different meshes

a)

b)
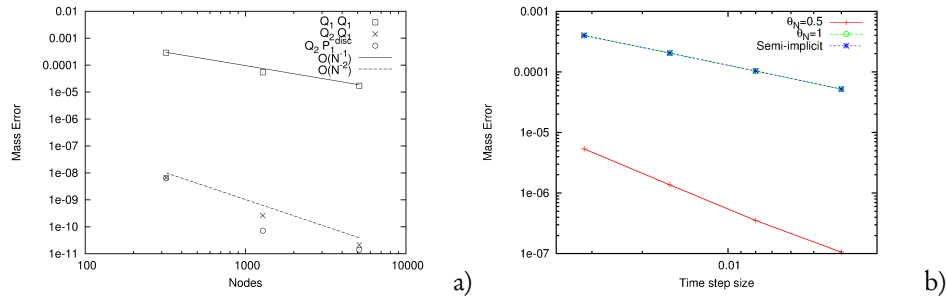
Figure 7. a) Global mass error related to spatial discretization for the stabilized Q_1Q_1-, Q_2Q_1- and $Q_2P_1^{\mathrm{disc}}$-element. b) Absolute change of mass at time $t = 0.8$ related to temporal discretization for the fully-implicit scheme with $\theta_N = 0.5$, $\theta_N = 1$ and the semi-implicit scheme.

behaviour to the $Q_2P_1^{\mathrm{disc}}$-element. Due to $\rho = 1$, the change of volume is equivalent to the change of mass. In order to focus on the error related to spatial discretization, we choose a very small time step $\Delta t = 10^{-6}$. We observe that the change of volume for the stabilized element is significantly larger (10^{-4}) compared to that for the stable elements (10^{-8}).

To have a closer look at the rates of convergence, we plot the mass error at time $t = 0.05$, for several refinement levels in Figure 7a). For the $Q_2P_1^{\mathrm{disc}}$- and Q_2Q_1-element the mass error goes to zero quadratically, i.e., with order 4 with respect to the mesh size h. The high order of convergence in the global mass error can be explained by the high order of regularity of the corresponding adjoint problem.

We find that for the stabilized Q_1Q_1-element, the mass error goes to zero linearly for increasing number of nodes, i. e., it is of order 2 with respect to the mesh size h. The results obtained for fully implicit, semi-implicit and explicit treatment of the free boundary are nearly identical. Due to the additional nonlinearity introduced by the Nitsche term, the Newton convergence in each time step is considerably slower for the implicit algorithm. On the other hand, we can use a larger time step Δt, such that in total the implicit method leads to a gain in efficiency.

In Figure 7b), we show the mass error related to time discretization for the fully-implicit scheme using $\theta_N = 0.5$ and $\theta_N = 1$ and the semi-implicit scheme at time $t = 0.8$. For spatial discretization, we used the Q_2Q_1-element and chose the mesh size fine enough such that the error related to time discretization is dominant. Clearly, the mass error goes down only linearly for the semi-implicit scheme and the implicit one when choosing $\theta_N = 1$. The absolute values for the change of mass are almost identical, but the sign of the error is different. For the fully implicit scheme with $\theta_N = 0.5$, the error in mass converges quadratically. Consequently, the fully implicit scheme with $\theta_N = 0.5$,
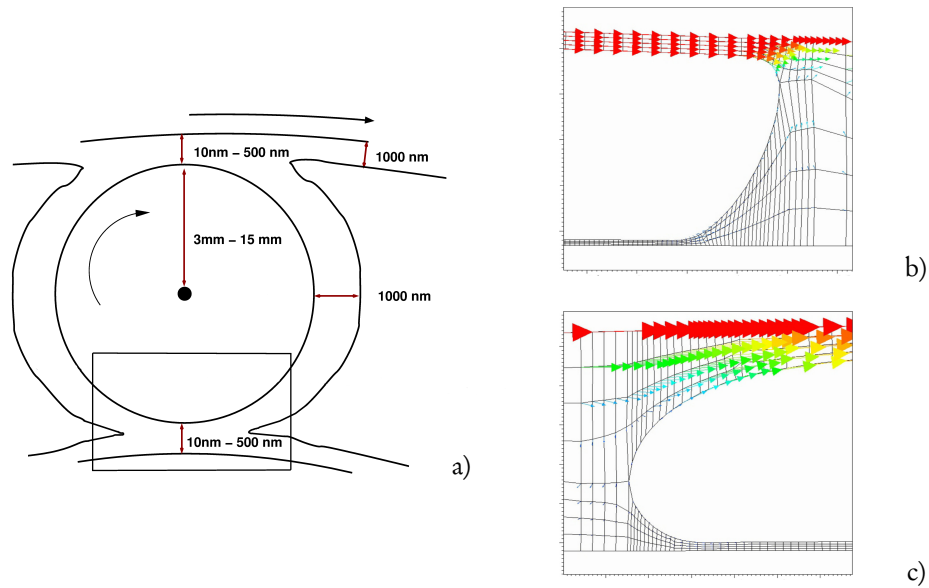
Figure 8. Extracts of the computational domain for simulations of one ball in a ball bearing a). Curved boundaries at inflow b) and outflow region c) as obtained by the free-boundary simulations.

is superior to the semi-implicit one with respect to mass conservation.

In this benchmark problem the physical oscillations occur for Reynolds numbers larger than approximately Re = 1.5. Clearly, the oscillations impose a restriction on the appropriate time step by its own. On the other hand, for lubrication flows the Reynolds number is typically much smaller than Re = 1 so that no oscillations occur and larger time-steps are possible. This is the situation where the fully implicit method is really advantageous. We close this section by presenting numerical results for a ball bearing geometry neglecting for a moment the effect of fluid-structure interaction. The velocity field near the menisci obtained for a ball bearing geometry is depicted in Figures 8b) and c).

A robust numerical treatment of the free boundary dynamics in lubrication flow is crucial for determining the distribution of the lubricant as, e.g., needed for calculations of oil consumption and its optimization. Here, a high order of approximation and thus small numerical diffusion of mass is particularly important.

5   Numerical results on ball bearing geometries

In this section, we show numerical results obtained for lubrication flow in ball bearings using the approaches described in the previous sections. It turns out that having a realistic geometry to start from, especially with respect to the initial position of the menisci, is essential for our simulation. Otherwise computation at higher entrainment velocities break down. For our application in mind, we need to be able to simulate entrainment velocities of up to 6000 rpm which corresponds to approximately 9.1m/s for a ball of radius 3mm and a contact angle of 18°.

In the following, we assume an initial geometry is given as the result of a free surface simulation. Our initial geometry has a minimal gap of $1.2 \cdot 10^{-7}$ m at the center of contact and a fluid film thickness up to $1.5 \cdot 10^{-6} m$ at the menisci. To study the effect of lubrication, we restrict ourselves to one ball in a bearing and a region near the center of contact between ball and race, which is chosen sufficiently large to cover the essential effects of interest (see Figure 8a)). Outside of this

region the velocity field is nearly identical to the velocity of the ball and pressure is negligible. We choose the coordinate system in such a way that the center of the ball is located at the origin. Thus, we are concerned with rotation of the ball, while the race undergoes only a translation. Further, we will make the assumption of "pure rolling", i.e., the radial velocity of the ball at the boundary equals the velocity of the corresponding race. Finally, we assume that a quasi-stationary state is reached after a certain time.

We use the monolithic ALE scheme descibed in (14), the Barus-Vogel law for the viscosity-pressure-temperature dependence and the compressibility modeling via the term introduced in Section 2.4. The boundary conditions for deformation, velocity and pressure in the fluid domain are as follows:

$$
\begin{aligned}
v_f &= v^D, & u_f &= u^D & &\text{on } \Gamma_{\text{oil}}, \\
n \cdot \sigma_f &= \gamma \kappa n, & \partial_n u &= 0 & &\text{on } \Gamma_f, \\
v_f &= v_s, & u_f &= u_s & &\text{on } \Gamma_{\text{FSI}},
\end{aligned}
\tag{59}
$$

where Γ_{oil} stands for the boundary at which the oil film is cut, Γ_f denotes the free boundary and Γ_{FSI} stands for the fluid-structure interface. The conditions on the FSI boundary $\Gamma_{\text{race}} \cup \Gamma_{\text{ball}}$ are incorporated via the continuity requirement of the trail functions, the term respresenting surface tension is calculated using the Laplace-Beltrami operator (51). The rotation of the ball and the translation of the race is taken into account via an L^2-projection of a given velocity v^D in the solid domain,

$$
(\hat{v}_s - \hat{F}_s^{-T} v^D, \phi^u)_{\hat{\Omega}_s} = 0 \quad \forall \phi^u \in U.
\tag{60}
$$

Furthermore, we include temperature as an additional variable according to Section 2.3 and preloading as described in Section 2.5. For discretization, we use the "inf-sup" stable $Q_2 P_1^{\text{disc}}/Q_2 Q_2$-element with biquadratic velocity, temperature and deformation coupled to linear discontinues pressures as well as the algorithm described in Section 3.3. As all boundaries are strongly curved, see e.g. Figure 8b) and c), all finite element approaches are iso-parametric (see Braack & Richter[10]).

The initial mesh corresponds to the situation at rest. At this state, ball and race are nearly in contact separated only by a very thin oil film. In our computational domain the distance at the closest point is about 10^{-7} m. On the other hand, the results of our simulations indicate that for high-speed situations the left and right meniscus are at a distance of up to 10^{-4} m from the center of contact. The use of isotropic cells in the fluid domain would thus be prohibitively expensive. Actually, we use a mesh with maximum cell-aspect ratio up to 400.

In the following, we will concentrate on two dimensional simulations. The material parameters we used for structure and oil are specified in Table ??. An extension to three dimensions is straightforward, in principle, but entails several technical complications, due to more complex mesh generation, higher storage requirements and longer computing times.

Figure 9 shows pressure, temperature and x-velocity profiles on the computational domain. The pressure profile shows a huge peak of almost 1 GPa near the center of contact. Outside the contact area the pressure is relatively small. In the structure pressure has no physical meaning and is simply defined by harmonic continuation. Starting from the inflow boundary on the left, the temperature profile reaches its maximum at the central point and a minimum behind it. Due to the high variations of pressure and velocity, the temperature shows considerable variations within the lubricant. The x-velocity takes its maximum before the central point. Near the left and right meniscus the normal velocity should be close to zero given the initial geometry is chosen sufficiently accurate.

Lubricant			
Density	ρ_0	800	kg/m^3
Surface Tension	γ	0.03	N/m
Barus-Vogel parameters	A	$1.034435 \cdot 10^8$	-
	C	2.144741	-
	m	2.942414	-
	$\alpha(\theta)$	$51.736 \cdot 10^{-9}$	m^2/N
		$-0.118\,\theta \cdot 10^{-9}$	
Heat conductivity	κ_c	0.16	W/(mK)
Heat capacity	c_P	2131	Ws/(kgK)
Bulk modulus	K	1	GPa
Heat transfer coefficient	$\alpha_{s/o}$	$5 \cdot 10^6$	-
Structure			
Young modulus	E	199.945	GPa
Poisson ratio	ν	0.25	-

**Table 1.** Material parameters of the lubricant oil and steel

5.1   The effect of compressibility

In Figure 10a), we compare the effect of using the exact ("physical") or the artificial compressibility prescription for a rotational velocity of 1.5 m/s. For the artificial compressibility, we used the parameter value $\epsilon = 10^{-14}$. For this value, and even smaller ones, adding compressibility has already a rather strong quantitative effect on the pressure profile compared to that obtained assuming "pure" incompressibility. Though, qualitatively the pressure profiles obtained for the different models appear similar the major difference is in the position of the pressure peak, which has also a strong influence on other quantities, e.g., the velocity field. For higher rotational velocities the differences in the pressure profiles corresponding to the different models increase, until finally there occur oscillations in the pressure profile for the artificial compressibility model and velocities bigger than 10m/s. For comparison, in Figure 10a), we have also plotted the pressure profile for constant viscosity $\mu \equiv \mu_0$. For constant viscosity a significantly larger region of negative pressure occurs where cavitation might take place. This effect, which seems to be suppressed by using either one of the compressibility models, lies outside the scope of the present article. For the numerical treatment of cavitation, we refer to Almqvist & Larsson[1] or Nilsson & Hansbo[30].

In Figure 10b), we compare the number of Newton iterations for the different regularization strategies. For comparison, we started the computations with an entrainment velocity of 0.05 m/s and increased the speed within the homotopy process by only 0.05 m/s per step. As stopping criterion, we used the reduction of the initial residual by a factor of 10^{-8}. In the regularization, we used the "physical" compressibility module $K = 10^9$ N/m^2 and the rather small "artificial" compressibility parameter $\epsilon = 10^{-16}$ and compare the results to those obtained for a rather small compressibility module $K = 10^{12}$ N/m^2 and an artificial compressibility parameter $\epsilon = 2 \cdot 10^{-15}$. This was the smallest value of ϵ for which we were able to get results up to rotational speed 9m/s. For bigger ϵ the artificial compressibility has significant impact on pressure, velocity and temperature. Further, we indicate the Newton convergence obtained for rather small values of both parameters, $\epsilon = 10^{-16}$ and $K = 10^{12}$ N/m^2. Even in these extreme cases, we still observe reasonable Newton convergence for rotational speeds up to 2 m/s. But we were not able to obtain any results for speeds bigger than 2.3 m/s. For the other two sets of parameter values, we observe similar behavior of the Newton iteration, which requires only between 2 and 6 iterations in each homotopy step. The small homotopy increment was chosen in order to get a fair comparison for
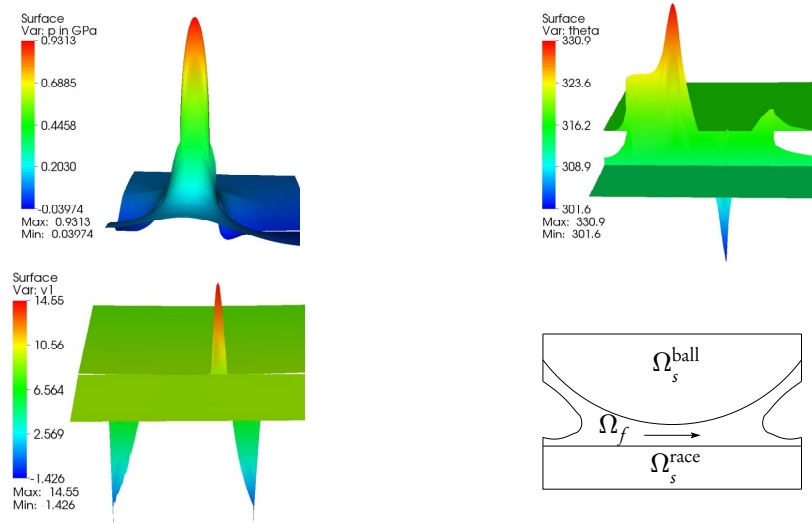
Figure 9. Pressure in GPa (top left), temperature in K (top right) and x-velocity (bottom left) in m/s plotted over the two dimensional computational domain where the race is in the front and the ball in the back part, $\theta_{\text{race}} = 313.15K$, $\theta_{\text{ball}} = 317.15K$ and a velocity of 6000 rpm ($\approx 9.1 m/s$). Bottom right: Scheme of the computational domain
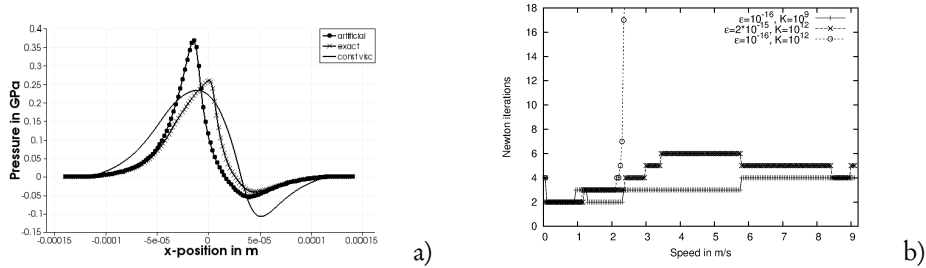

Figure 10. a) Pressure profiles along a line through the fluid domain computed by using "artificial" compressibility, "exact" (physical) compressibility and constant viscosity. b) Number of Newton iterations for "artificial" compressibility, "exact" compressibility and "pure" incompressibility

all the three sets of parameters. Actually, within the homotopy method described in Section 3.3 using the "physical" compressibility with a small ϵ, it was possible to use a ten times bigger homotopy increment.

5.2 Study of mesh convergence

Before proceeding to the computation of the physically interesting quantities in ball bearings, we want to investigate the accuracy, which can be achieved on the spatial meshes used in our simulations. To this end, we realize computations on a rather coarse mesh consisting of 30 032 cells and on meshes obtained by one or two global uniform refinements steps consisting of 120 128 cells and 480 512 cells. In Figure 11a) and b), we show the pressure profiles and the profile of the deformation of the race for an entrainment velocity of 9.1m/s, respectively, obtained on these meshes. This velocity corresponds to 6 000 rpm, the maximum working speed of the bearings. For both quantities, we observe good agreement on all meshes, i.e., the spatial discretization is
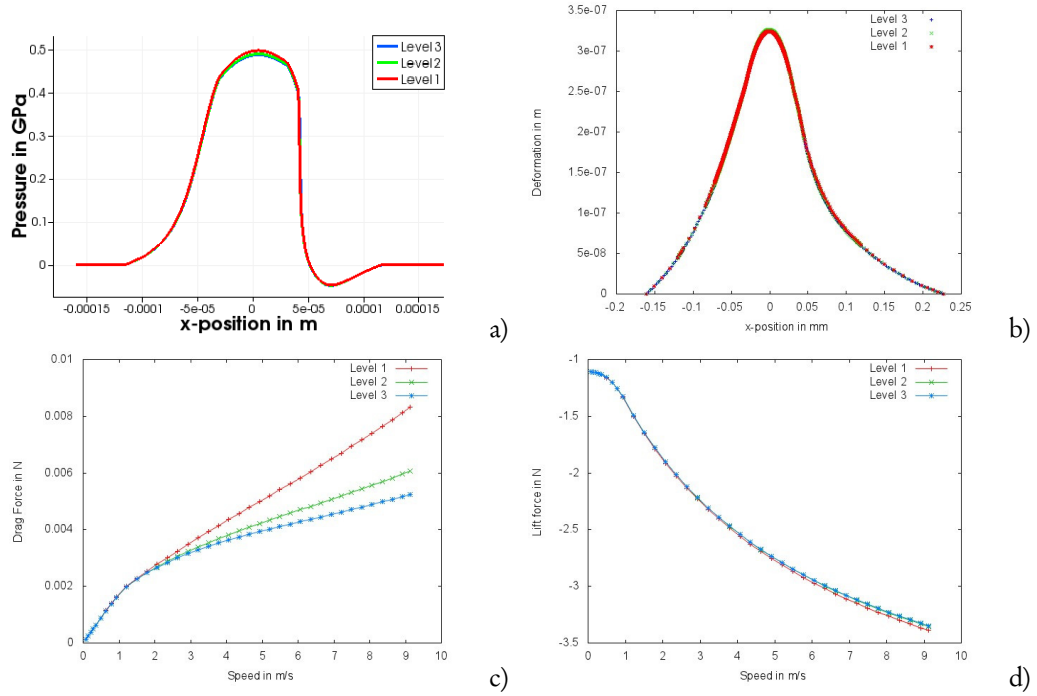
Figure 11. Pressure a) and deformation profile of the ball b) for a high-speed simulation (9.1m/s), drag c) and lift d) forces over entrainment velocity, obtained on three different levels of successive mesh refinement

converged. Furthermore, in Figure 11c) and d), we plot the drag and lift forces

$$c_{\text{drag}} := \int_{\Gamma_{\text{ball}}} t \cdot \sigma_f \cdot n \, ds, \quad c_{\text{lift}} := \int_{\Gamma_{\text{ball}}} n \cdot \sigma_f \cdot n, \tag{61}$$

acting on the ball as functions of the entrainment velocity. For the lift force, we observe a satisfactory convergence behaviour. The values on the finer meshes are almost identical, while the values obtained on the coarse mesh deviate slightly for higher rotational velocities. The drag force is a lot more sensitive and difficult to compute. Here, the values obtained on the coarse mesh do not seem to provide a reasonable approximation at all for rotational velocities larger than 3m/s. We remark that on this mesh the fluid domain Ω_f is covered by only 4 cells in vertical direction. This is by far too little resolution for getting reasonable approximations for the velocity gradient, which is the dominant part of the contribution of σ_f to the drag force.

5.3 Computation of relevant physical quantities

First, we study the dependence of the lubricant film thickness with respect to the rotational speed. For minimal and central film thickness, we compare our results with those obtained from the analytical Hamrock-Dowson-Formula (Hamrock et al. [18]), which is widely used within the engineering community and has been validated by many experiments (see, e.g., Krupka et al. [29]). Figure 12 shows our numerical results and those by this formula for preloading of 0.5 N and 5 N and different inflow velocities. For considerably larger preloading the modeling error due to our simplified treatment of preloading becomes too large such that a quantitative agreement cannot be expected anymore (see Section 2.5). The central film thickness obtained by our computation is in almost perfect agreement with the analytical theory. Only for very small rotational velocity the
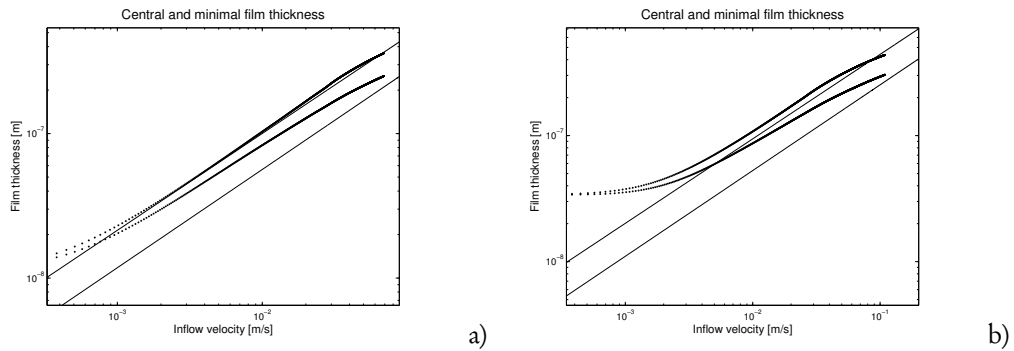
Figure 12. Central and minimal film thickness for preloading $0.5\,N$ a) and $5\,N$ b). "Solid lines" are the values obtained from the Hamrock-Dowson formula and "dots" are our computed values.
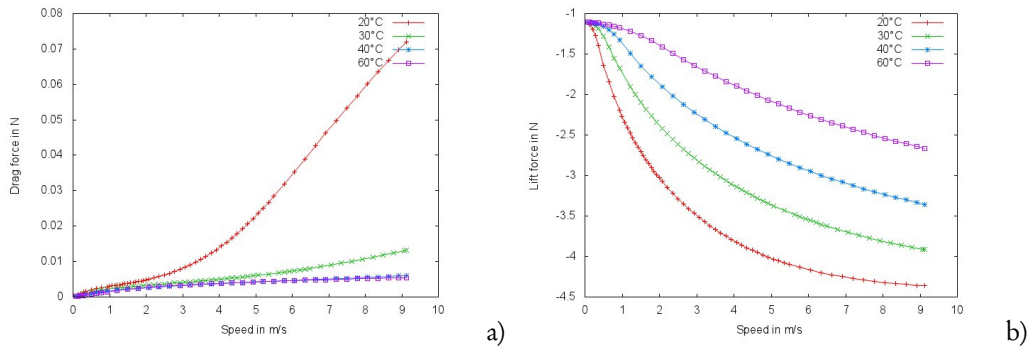

Figure 13. Dependence of drag a) and lift b) force on the rotational speed for temperatures of $20, 30, 40$ and $60°C$ in the race

curves deviate considerably. This happens in a region of film thicknesses of about $10\,nm$, where any kind of modeling based on continuum assumptions seems dubious.

Next, we consider the influence of temperature on the frictional forces. In Figure 13, we show drag and lift force values for different temperatures in ball and race. Here, the ball is assumed to be $0.5°C$ warmer than the race while the temperature in the race is $20, 30, 40$ and $60°C$. While former approaches simulating the elastohydrodynamic behavior of lubricant films fails for temperatures as small as $20°$ C, our proposed numerical scheme is robust for the complete range of physical relevant temperature and velocity values.

The drag force seems quite unsensitive to temperature variations above $40°C$. But, below $40°C$ the drag force increases rather quickly for high rotational speed. For temperatures below $0°C$ our numerical simulation became unstable. The lift force shows a more uniform monotone dependence on temperature.

Finally, we compare the loss torque for a realistic configuration and compare our results to analytical models developed by our industrial partner Rockwell Collins Germany GmbH. Details of this comparison will be given in a forthcoming paper. Although, we concentrated on a relatively small part of a ball bearing domain in our computations, the results shown in Figure 14 show good qualitative agreement.
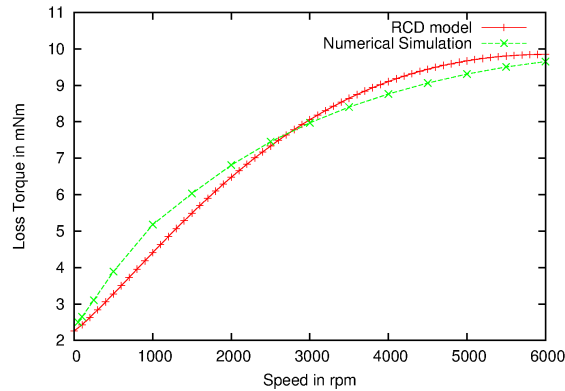
Figure 14. Loss torque computed from analytical models developed by Rockwell Collins Germany GmbH compared to our simulation results

6 Conclusion

In this article, we propose a framework for detailed finite element simulations of elastohydrodynamic lubrication in ball bearings. We introduced a novel solution method, which treats the evolution of the free boundary fully implicitly and therefore does not suffer from the usual time step-size restriction. We validated our approach by applying it to a benchmark problem from the literature and also used it for a ball bearing configuration. We compared different finite element discretizations with respect to the error in mass conservation. In our numerical tests both "inf-sup" stable $Q_2 Q_1$- and $Q_2 P_1^{\mathrm{disc}}$-elements showed excellent performance. Further, we found that in time discretization the fully-implicit scheme leads to higher-order accuracy in the conservation of mass compared to algorithms previously used in literature which treat the evolution of the free boundary explicitly or semi-implicitly.

For the elastohydrodynamic lubrication problem, we developed a fully monolithic ALE method including local thermal effects by means of an additional variable. We showed that our approach gives reasonable results in terms of film thickness, frictional forces and loss torque. Despite the variety of numerical challenges present in this application, our approach showed robustness also for situations with high rotational speed. We described the ingredients of our numerical method in detail and particularly investigated the gain of pressure regularization by allowing for some degree of compressibility in the model. We found that the size of the regularization parameter ϵ has to be chosen carefully if artificial compressibility is needed at all. Finally, we demonstrated the importance of including thermal effects in computing frictional forces.

In this article, we used the Navier-Stokes equations for a non-Newtonian-fluid which is governed by a Barus-Vogel law and a St. Venant-Kirchhoff material for the structure. Our method, however, is flexible and robust with respect to fluid and structure models, geometry and parameters. The results presented here are exemplary and the numerical algorithm easily carries over to other types of lubrication problems with different fluids. While parts of the experimental data can be matched precisely by analytical approximations such as the Hamrock-Dowson formula, numerical methods are able to predict nearly every quantity of interest like drag and lift, film thickness profiles or heat transfer for which no analytical formula is available.

References

[1] T. Almqvist and R. Larsson. The Navier-Stokes approach for thermal EHL line contact solutions. *Tribology International*, 35:163–170, 2002.

[2] Chandrasekhar Annavarapu, Martin Hautefeuille, and John E. Dolbow. A robust Nitsche's formulation for interface problems. *Comput. Methods Appl. Mech. Engrg.*, 225 – 228(0):44 – 54, 2012.

[3] Thomas Apel, Tobias Knopp, and Gert Lube. Stabilized finite element methods with anisotropic mesh refinement for the Oseen problem. *Appl. Numer. Math.*, 58(12):1830–1843, 2008.

[4] Eberhard Bänsch. Finite element discretization of the Navier-Stokes equations with a free capillary surface. *Numer. Math.*, 88(2):203–235, 2001.

[5] Guy Bayada and Michèle Chambat. The transition between the Stokes equations and the Reynolds equation: a mathematical proof. *Appl. Math. Optim.*, 14(1):73–93, 1986.

[6] R. Becker and M. Braack. A finite element pressure gradient stabilization for the Stokes equations based on local projections. *Calcolo*, 38(4):173–199, 2001.

[7] R. Becker, M. Braack, D. Meidner, T. Richter, and B. Vexler. The finite element toolkit Gascoigne. http://www.gascoigne.uni-hd.de.

[8] T. Belytschko. Fluid-structure interaction. *Comput. Struct.*, 12:459–469, 1980.

[9] M. Braack. A stabilized finite element scheme for the Navier-Stokes equations on quadrilateral anisotropic meshes. *M2AN Math. Model. Numer. Anal.*, 42(6):903–924, 2008.

[10] M. Braack and T. Richter. Solutions of 3D Navier-Stokes benchmark problems with adaptive finite elements. *Computers and Fluids*, 35(4):372–392, May 2006.

[11] J. U. Brackbill, D. B. Kothe, and C. Zemach. A continuum method for modeling surface tension. *J. Comput. Phys.*, 100(2):335–354, 1992.

[12] V Bruyere, N Fillot, G.E Morales-Espejel, and P Vergne. Computational fluid dynamics and full elasticity model for sliding line thermal elastohydrodynamic contacts. *Tribology International*, 46(1):3–13, 2012.

[13] W. Dettmer and D. Perić. A computational framework for free surface fluid flows accounting for surface tension. *Comput. Methods Appl. Mech. Engrg.*, 195(23-24):3038–3071, 2006.

[14] Th. Dunne, R. Rannacher, and Th. Richter. Numerical simulation of fluid-structure interaction based on monolithic variational formulations. In *Fundamental trends in fluid-structure interaction*, volume 1 of *Contemp. Chall. Math. Fluid Dyn. Appl.*, pages 1–75. World Sci. Publ., Hackensack, NJ, 2010.

[15] M. Franta, J. Málek, and K. R. Rajagopal. On steady flows of fluids with pressure- and shear-dependent viscosities. *Proc. R. Soc. Lond. Ser. A Math. Phys. Eng. Sci.*, 461(2055): 651–670, 2005.

[16] V. Girault and P.-A. Raviart. *Finite Elements for the Navier Stokes Equations*. Springer, 1986.

[17] R. Gohar. *Elastohydrodynamics*. World Scientific Publishing, Singapore, 2nd edition, 2001.

[18] B. Hamrock and D. Dowson. Isothermal elastohydrodynamic lubrication of point contacts. Tech. rep., NASA, 1976.

[19] B.J. Hamrock, S.R. Schmid, and B.O. Jacobson. *Fundamentals of fluid film lubrication*. Marcel Decker, Inc., New York, Basel, 2 edition, 2004.

[20] Anita Hansbo and Peter Hansbo. An unfitted finite element method, based on Nitsche's method, for elliptic interface problems. *Comput. Methods Appl. Mech. Engrg.*, 191(47–48): 5537 – 5552, 2002.

[21] D.E. Hart, M. Berzins, C.E. Goodyer, and P.K. Jimack. Using adjoint error estimation techniques for elastohydrodynamic lubrication line contact problems. *Internat. J. Numer. Methods Fluids*, 67:1559–1570, 2011.

[22] Heinrich Hertz. Über die Berührung fester elastischer Körper. *Journal für die reine und angewandte Mathematik*, 92:156–171, 1882.

[23] C.W. Hirt, A.A. Amsden, and J.L. Cook. An arbitrary lagrangian-eulerian computing method for all flow speeds. *Journal of Computational Physics*, 14:227–469, 1974.

[24] J. Hron and S. Turek. A monolithic FEM/multigrid ssolver for an ALE formulation of fluid-structure interaction with applications in Biomechanics. In J.-J. Bungartz and M. Schäfer, editors, *Fluid-Structure Interaction*, pages 146–170. Springer, Berlin Heidelberg, 2006.

[25] T. J. R. Hughes and A. N. Brooks. Streamline upwind/Petrov-Galerkin formulation for convection dominated flows with particular emphasis on the incompressible navier-stokes equation. *Comput. Methods Appl. Mech. Engrg.*, 32:199–259, 1982.

[26] Thomas J. R. Hughes, Leopoldo P. Franca, and Marc Balestra. A new finite element formulation for computational fluid dynamics. V. Circumventing the Babuška-Brezzi condition: a stable Petrov-Galerkin formulation of the Stokes problem accommodating equal-order interpolations. *Comput. Methods Appl. Mech. Engrg.*, 59:85–99, 1986.

[27] I. Jubault, J. Molimard, AA Lubrecht, JL Mansot, and P. Vergne. In situ pressure and film thickness measurements in rolling/sliding lubricated point contacts. *Tribology Letters*, 15(4): 421–429, 2003.

[28] Stefan Knauf. *Numerical Simulations for ball bearings considering fluid-structure-interaction problems and non-Newtonian fluids with a free boundary*. PhD thesis, Ruprecht-Karls-Universität Heidelberg, 2011.

[29] I. Křupka, M. Hartl, and M. Liška. The influence of contact pressure on central and minimal film thickness within ultrathin film lubricated contacts. *Journal of Tribology*, 127:890–892, 2005.

[30] B. Nilsson and P. Hansbo. A Stokes model with cavitation for the numerical simulation of hydrodynamic lubrication. *International Journal for Numerical Methods in Fluids*, 67(12): 2015–2025, 2011.

[31] J. Nitsche. Über ein Variationsprinzip zur Lösung von Dirichlet-Problemen bei Verwendung von Teilräumen, die keinen Randbedingungen unterworfen sind. *Abh. Math. Sem. Univ. Hamburg*, 36:9–15, 1971.

[32] N. Ohno, N. Kuwano, and F. Hirano. Bulk modulus of solodified oil at high pressure as predominant factor affecting life of trust ball bearings. *Tribology Transactions*, 38:285–292, 1995.

[33] K. R. Rajagopal and A. Z. Szeri. On an inconsistency in the derivation of the equations of elastohydrodynamic lubrication. *R. Soc. Lond. Proc. Ser. A Math. Phys. Eng. Sci.*, 459(2039): 2771–2786, 2003.

[34] M. Souli and J.P. Zolesio. Arbitrary lagrangian eulerian and free surface methods in fluid mechanics. *Comput. Methods Appl. Mech. Engrg.*, 191(3–5):451 – 466, 2001.

[35] T.E. Tezduyar, S. Mittal, S.E. Ray, and R. Shih. Incompressible flow computations with stabilized bilinear and linear equal-order-interpolation velocity-pressure elements. *Computer Methods in Applied Mechanics and Engineering*, 95:221–242, 1992.